

Alma Mater Studiorum Università di Bologna  
Archivio istituzionale della ricerca

Time-Space Evolution of the Groningen Gas Field in Terms of b-Value: Insights and Implications for Seismic Hazard

This is the final peer-reviewed author's accepted manuscript (postprint) of the following publication:

*Published Version:*

Gulia, L. (2023). Time-Space Evolution of the Groningen Gas Field in Terms of b-Value: Insights and Implications for Seismic Hazard. SEISMOLOGICAL RESEARCH LETTERS, 94(4), 1807-1820 [10.1785/0220220396].

*Availability:*

This version is available at: <https://hdl.handle.net/11585/939938> since: 2024-01-10

*Published:*

DOI: <http://doi.org/10.1785/0220220396>

*Terms of use:*

Some rights reserved. The terms and conditions for the reuse of this version of the manuscript are specified in the publishing policy. For all terms of use and more information see the publisher's website.

This item was downloaded from IRIS Università di Bologna (<https://cris.unibo.it/>).  
When citing, please refer to the published version.

(Article begins on next page)

This is the final peer-reviewed accepted manuscript of:

Laura Gulia; Time–Space Evolution of the Groningen Gas Field in Terms of b-Value: Insights and Implications for Seismic Hazard. Seismological Research Letters 2023; 94 (4): 1807–1820.

The final published version is available online at:  
<https://doi.org/10.1785/0220220396>

#### Terms of use:

Some rights reserved. The terms and conditions for the reuse of this version of the manuscript are specified in the publishing policy. For all terms of use and more information see the publisher's website.

*This item was downloaded from IRIS Università di Bologna (<https://cris.unibo.it/>)*

***When citing, please refer to the published version.***

1 Time-space evolution of the Groningen gas field in terms of b-value:  
2 insights and implications for seismic hazard.

3  
4 Laura Gulia<sup>1\*</sup>  
5

6 <sup>1</sup> University of Bologna, Department of Physics and Astronomy, Bologna.

7 L. Gulia: Laura Gulia (laura.gulia@unibo.it)  
8

9 ***Declaration of Competing Interests***

10 The author acknowledges there are no conflicts of interest recorded  
11

12 ***Abstract***  
13

14 The Groningen gas field, located in the north-east of Netherlands, is the Europe's largest  
15 onshore gas field. It was discovered in 1959 and production started in 1963: continuous  
16 production leads to reservoir compaction and subsidence, gradually loading pre-existing  
17 fault and induced seismicity started about 30 years into the production. The seismic  
18 hazard and risk related to the induced seismicity is determined not only the rate of  
19 activity, but it is equally influenced by the relative size distribution of the seismicity, the  
20 b-value. I re-analyze the spatial and temporal evolution of the b-value in the field using  
21 an alternative approach to overcome magnitude in completeness heterogeneity and link  
22 it to the evolution of fault loading and subsidence. Spatial variations of b-values are found  
23 to vary between 0.61 and 1.3, with lowest observed values observed in the location of the

2012 Huizinge M3.6 earthquake. In the last 10 years, the mapped b-value are more homogeneous throughout the field.

The spatial and temporal evolution of the b-value in the field is shown in this study to be quite complex and systematically linked it to the evolution of fault loading, absolute compaction and the rate of compaction, an important finding that offers new insights into hazard reduction and mitigation strategies of extraction relation induced seismicity. Compaction rates below 2 mm/year are not correlated to seismicity above M 2.0 in the history of the field, suggesting that low volume production may be safer than previously assumed.

## ***Introduction***

Anthropogenic activities lead to an increasing number of induced phenomena, including earthquakes. In the case of gas-production, extraction of mass and depletion of the pressure cause reservoir compaction, a process accompanied by both seismicity and surface subsidence (e.g., Segall, 1992; Zoback, 2007); these related processes show a delay with respect to gas extraction and the strict link between production, compaction and seismicity has been established in numerous studies (Bourne et al., 2014; Van Thienen-Visser and Fokker, 2017; Hol et al., 2018; Smith et al., 2019; Mehranpour et al., 2021).

The prime example of gas extraction related induced seismicity is the Groningen field in the Northwestern part of the Netherlands, the largest known gas field in the Western Europe and for many years the major supplier of natural gas to the Northwestern

European market (van Thiessen-Visser and Brunese, 2015). The gas is stored in the Permian Rotliegend sandstone, a shallow reservoir at a depth of about 3000 m, overlaid by a layer of Zechstein salt deposit (De Jager and Visser, 2017). The region is close to or even below sea level, thus surface subsidence, that has been measured already since one year after the beginning of gas production, is a substantial concern.

During production, mass is removed, fluid pressures are reduced, and the reservoir compacts; differential compaction rates gradually load pre-existing faults. About 1500 faults have been mapped so far from extensive 3D seismic surveys (NAM, 2016) and the predominant style-of-faulting of the field, derived from focal mechanisms (Willacy et al., 2019), is normal: gas extraction increases the effective vertical stress and thus the differential stress. Consequently, some faults can increasingly become unstable nucleating earthquakes: seismicity is indeed associated with the re-activation of normal faults, NW–SE trending, at reservoir level. Zbinden et al. (2017) provide a good review of the physical processes involved, including not only subsidence but also 2 phase flow between reservoir compartments and suggest three mechanism that influence the stress path that a fault undergoes during production:

1. The compaction of the reservoir leads to rotation of the principal stresses, which increases the shear stress in the fault zone.
2. The pressure drop in the gas reservoir strongly affects the horizontal and vertical stress acting on the fault through poroelastic effects, leading to an increase in differential stress and thus to an increase in shear stress.
3. Fluid flow into and out of the fault zone strongly affects the pore pressure evolution, hence altering the effective normal stress acting on the fault.

74

75 The induced seismicity related to the production causes considerable concern and  
76 anxiety in the population and increases the seismic risk in this previously almost a-  
77 seismic region: 1487 events with a maximum magnitude of Ml 3.6 have been recorded in  
78 the field from December 5, 1991, to May 22, 2022. The shallow surface in the area consists  
79 of thick layers of very soft deposits and the buildings have been designed and constructed  
80 without consideration for the horizontal loads typically experienced during an  
81 earthquake (van Elk et al., 2019): moderate magnitude events, such as the August 16,  
82 2012, Huizinge Ml 3.6, can cause both significant non-structural damages to buildings and  
83 safety concerns for residents. Hazard and seismic risk assessment related to gas  
84 production became a priority in the following years.

85

86 One of the most important ingredients of hazard is the extrapolation of the observed  
87 frequency magnitude distribution, the b-value of the Gutenberg and Richter relationship  
88 (Gutenberg and Richter, 1944; Ishimoto and Ida, 1939), to larger magnitudes. It is one of  
89 the fundamental empirical laws of seismology and it estimates the number of  
90 earthquakes  $N$  larger than or equal to magnitude  $M$ , via the formula  $\log(N) = a - bM$ ,  
91 whereby the *a-value* is a volume productivity measure, and the *b-value* quantifies the  
92 frequency-magnitude distribution (FMD) slope.

93

94 The b-value can be seen simply as an empirical fitting parameter that may be a constant,  
95 or variable with space and time. However, a wide body of research has documented that  
96 the changes in b-values are related to physics-based principles. Interpreting b-values in  
97 the physics-based framework can hence be a tool to better understand the reservoir  
98 evolution, it maybe also be the key to enhance the forecasting ability. A key concept is

the inverse correlation between b-value and differential stress, widely documented, both by laboratory specimens (from Scholz, 1968) and by observations in natural environments (Schorlemmer et al., 2005; Tormann et al., 2015; Gulia and Wiemer, 2010, 2019; Petrillo et al., 2020; Scholtz, 2015). For injections related induced seismicity Bachmann et al. (2012) and Goertz-Allman and Wiemer (2013) have shown that b-values in the highest pore pressures areas are much higher than observed at greater distances from the injection well. For natural seismicity, the stacking of the b-value time-series for 31 seismic sequences from well-monitored regions (Gulia et al., 2018) revealed a systematic b-value increase of about 20% in the proximity of the fault after a M6+; several single case studies (Papadopoulos et al., 2010; Tormann et al., 2015, 2014; Gulia and Wiemer, 2019, 2021; Gulia et al., 2016, 2020) investigated the b-value decreasing preceding the mainshock. All these findings are consistent with the inverse dependency of b-value with differential stress: the higher the applied differential stress, the lower the b value and vice versa.

In the case of Groningen, the b-value time-space variations should therefore reflect differential stress changes in the field that are driven by subsidence and compaction-generated stress-re-distribution. In this study, I first reconstruct the evolution in space and time of the b-value in the field and interpret it in terms of stress evolution. Finally, I reinvestigate, enrich, and discuss the correlation between compaction and b-value, first shown by Bourne et al. (2014).

### ***Production and seismicity in the Groningen gas field***

123 The Groningen gas field was discovered in 1959 and production started in 1963; the  
124 region was considered aseismic till 1991, when the first earthquake (Ml 2.3) occurred.  
125 Until 2003, seismicity was low and mainly located at the center of the field, the region  
126 where extraction was concentrated. Starting from 2003, due to the rising market demand,  
127 the production increased, and the number and magnitude of events started to increase  
128 too, till the occurrence of a Ml 3.6 event in 2012, that caused substantial non-structural  
129 damages and greatly increased the level of anxiety (Muntendam-Bos et al., 2017),  
130 together with the observed exponentially increasing trend in seismicity. Seismicity  
131 increased passing from 2 events with  $M \geq 1.5$  events in 2001 to 29 events  $M \geq 1.5$  in  
132 2013 (Muntendam-Bos et al., 2021). Starting from 2014, after an investigation by the  
133 State Supervision of Mines (Muntendam-Bos and De Waal, 2013) that showed an  
134 increased risk for larger events due to gas extraction, production measures aimed at  
135 lowering the level of seismicity have been implemented and the production has been  
136 gradually reduced by 80% in the central part of the field and instead moved towards the  
137 South. The adopted measures appear to be successful, and they resulted in a reduction of  
138 the total number of events in the field: about 65% reduction of the seismicity rates in the  
139 center of the field (from 0.42 events  $\text{km}^2/\text{yr}$  in 2013 to 0.15 events  $\text{km}^2/\text{yr}$  in 2015), but  
140 an acceleration in the southwest (from 0.14 events  $\text{km}^2/\text{yr}$  in 2013 to 0.24 events  $\text{km}^2/\text{yr}$   
141 in 2014; Muntendam-Bos, 2020). The expectation by the operator Nederlandse Aardolie  
142 Maatschappij BV (NAM) and regulator, the Dutch State Supervision of Mines (SodM),  
143 however, were that this reduction in seismicity would be a temporary relieve only, with  
144 continued production in the south, it was expected that the rate of seismicity would again  
145 increase. Despite the measures taken, a Ml 3.4 occurred near Zeerijp, NE part of the field,  
146 in January 2018. The continuing seismicity and the continued public opposition in the  
147 Groningen area notched the Dutch government to decide to further reduce gas

production, proposing a complete stop in 2030. This roadmap was further accelerated in 2020, and the termination of production has now been anticipated to 2023.

### ***State of the art on b-value in the Groningen gas field***

***Spatio-temporal variations of b-value*** - In the last decade, an increasing number of papers investigated the effects of gas production on seismicity; among them, some analysed the spatial and temporal variations of b-value. Below I summarise the key findings of these studies.

The spatial variability of b-value have been investigated in a report by Harris and Bourne (2015): they first show that the b-value of the overall catalogue is consistent with the commonly accepted value of 1.0 for the period 1st May 1995 to 31st December 2014; then they focus on two subregions of 5-km radius centred around two locations characterized by different production – Loppersum and Ten Boer – finding that in the area around Ten Boer the b-value is still consistent with 1, but in Loppersum, the subregion with the most intense seismicity, it is significantly lower. To test whether significant temporal shifts are present, each sub-catalogue is then divided in two parts of equal length and the b-values of the two time periods compared. Till 2014, between the first and second halves of the catalogues for the two sites, there are no temporal variations. b-value variations for various periods and parts of the field have been confirmed by other studies (Wentinck, 2015; Bourne and Oates, 2017). Muntendam-Bos and Grobbe (2022) confirm the statistically significant spatial variations of b-value but find no statistical evidence of a temporal variation.

Muntendam-Bos et al. (2017) study whether both theory and models derived from observations of b-values in natural contexts could be adopted in hydrocarbon-production-induced seismicity. To answer this question, the authors analyse the temporal evolution of the b-value plotting the time-series of all the events recorded in the field, with different sample sizes; the spatial variability is not considered. Their plots show that before the occurrence of the biggest events in the field (2012), the b-value increases instead of decreasing: the consequent probability of a larger-magnitude event decreases before the occurrence of this quake. The authors conclude that *for short-term earthquake prediction by hydrocarbon-production-induced seismicity these types of analysis could be misleading.*

The Royal Netherlands Meteorological Institute (KNMI) progressed from simply monitoring the larger felt events to quantifying hazard and giving relevant input to exploration regulations (Dost et al., 2012). The probabilistic seismic hazard analysis conducted by KNMI (Dost and Spetzler, 2015; Spetzler and Dost, 2017) adopts a seismic source model based on recorded seismicity and performs an integration over seismic zones, following Cornell (1968). Due to the time-space b-value variations shown by Harris and Bourne (2015), different b-value were calculated for each seismic zone, that passed from four (Dost and Spetzler, 2015) to three (Spetzler and Dost, 2017).

***b-value and compaction*** - Geodetic monitoring of subsidence over the field began in 1964 with optical levelling over a limited network in the central and southern part of the field (Bourne et al., 2014). In 1972, network coverage was extended to the entire field and the number of benchmarks increased; the subsidence rate accelerated after 1975 (van Thienen-Visser and Fokker, 2017). Bourne et al. (2014) superimposed the

epicentres of the events in the field on the reservoir compaction maps for different time intervals and noted the concentration of events within the region of greatest compaction, implying that the occurrence of earthquakes, in space and time, is influenced by the reservoir compaction. The authors labelled each event according to the reservoir compaction at the event's origin time and epicentre, then grouped subsets of events within a range of compaction values, requiring a minimum number of 50 events. The resulting plot (Figure 14 in Bourne et al., 2014) shows a compelling inverse correlation between b-value and compaction. This correlation has important implications on the future project of seismic hazard and risk and the forecasted decrease of the b-value with increasing compaction, is a major driver of the seismic hazard in continued production.

## ***Data***

The datasets used in this work are part of the data package provided by NAM to the presenters at the Groningen Mmax Workshop II (Bommer and van Elk, 2017), held in Amsterdam on June 2022, following the broad principles of the SSHAC (Senior Seismic Hazard Analysis Committee) guidelines for hazard assessment. The seismic catalogue contains 1487 events collected by the Royal Netherlands Meteorological Institute (KNMI) in the period 5 December 1991- 22 May 2022; the original location of the KNMI seismic stations have been converted from latitude and longitude to the standard system for The Netherlands – RDS, expressed in terms of Easting and Northing coordinates (meters). KNMI assumes a focal depth of 3km, which is the average depth of the gas reservoir.

The seismic network, fully operating since 1995, was designed to detect and locate earthquakes of magnitude (MI) 1.5 and larger (Dost et al., 2017); densification of the monitoring network resulted in a decrease of the location threshold and magnitude of completeness, that passed from 1.2 in the period April 2003-August 2012, to 0.8 in the period August 2012-August 2014, reaching the current value of 0.5 since September 2014 (Dost et al., 2017; Paleja and Bierman, 2016). Since the network was not altered before 2010, the same  $M_c$  of 1.2 can be assumed also for the years preceding 2003 (Muntendam-Bos, 2020). The compaction model for the field adopted in this work, included in the data package provided by NAM, is calibrated on the V6 scenario, operational strategy 2 (OS2; NAM 2021): the reservoir compaction is expressed as a function of both spatial position and time since the start of production. Figure 1 shows a summary of the network evolution with time.

## ***Method and Results***

***b-value changes: Radial analysis*** - To increase the robustness of the analysis, two different methods to estimate b-values are used in this study: the first one is the formula by Aki (1965), corrected by Utsu (1966) for binned magnitudes (from now on, AU66), that relies on a robust and accurate estimate of the magnitude of completeness,  $M_c$ . As an alternative method, the b-value estimator proposed by van der Elst (2021; from now on, vde21) is also applied. The vde21 estimator does not require an accurate estimate of  $M_c$  and allows to calculate b-value on datasets with a certain amount of incompleteness as well as on datasets with variable levels of completeness in time. van der Elst (2021) shows that the distribution of magnitude differences is identical to the distribution of magnitudes, but with no reference to a minimum magnitude, and that the positive subset of the differences

between successive earthquakes is minimally biased by changing catalog completeness. This new estimator is insensitive to transient changes in catalog completeness and offers robust b-value estimations even during active earthquake sequences, (van der Elst, 2021) characterised by periods of strong incompleteness (Kagan, 2004).

The differential stresses on faults are changing substantially with space and time during production (e.g., Zbinden et al., 2017). Given the inverse correlation between b-value and differential stress, we should expect in the Groningen field both spatial and time variations of not only the activity rate (already well documented) but also of the b-value. The lowest b-values should be observed in the region of highest differential stress concentration, hence near the area where production was concentrated till 2014 and where also the largest event of Ml 36 has occurred. The highest b-values, in contrast, should be observed on the fringes of the fields. Such spatial variation should be time-dependent, reflecting gradually loading with time but also changes in the production: after 2014, when production is greatly reduced in the central part of the field and shifted southward, the b-values in the central part should remain constant and those in the surrounding areas should decrease. Figure 2 summarizes this conceptual expectation.

Because spatial and temporal variations of b-values are expected, but at the same time the dataset is very limited to resolve them, the choice of the right mapping approach is important. Spatial variations can be best evaluated by mapping b-value on a dense grid (Tormann et al., 2014), and robust estimations require typically a minimum number of 50 to 150 events above the magnitude of completeness (Wiemer and Wyss, 2000). Biases in b-value estimation also need to be carefully considered (Gulia et al., 2022; Gulia and

Wiemer, 2021); to also understand the temporal evolution, one would ideally investigate maps at different times.

To address the limits imposed by the size of the dataset while targeting the expected main gradients (Figure 2), I analyse first the seismicity in non-overlapping spherical volumes around the largest event (Huizinge, Ml 3.6 in 2012). I analyse two different periods, before and after the change in production in 2014, thus comparing the periods 01/1991-12/2013 and 01/2014- 05/ 2022. I sample events in the smallest radius that allows estimating a robust b-value, which corresponds to the volume containing a minimum number of 50 events above Mc. Considering the Mc established in previous work (Dost et al., 2017; Paleja and Bierman, 2016), the minimum radius for estimating b-values around the epicentre of the Huizinge event is about 4 km. Figure 3 shows the FMDs of the 4 doughnut-shaped volumes for the two time periods. In period 1, the b-value increase systematically from 0.61 for the central area, to  $b=1.3$  for the outmost circle, events 12 – 20 km from the epicentre. For period 2, the central events show a similar b (0.67), but b-values of out segments have decrease considerably to values around 0.85. Figure 4 a-b summarizes the same observations, color-coded onto the theoretical scheme of Figure 2. The two plots in Figure 4 c-d compares the b-values as a function of distance calculated by AU66 and the ones estimated by vde21. Both shows the same trend and agree each other within the uncertainty, except for the volume 12-20 km, for which AU66 results in significantly higher estimates: this volume groups parts of the field, characterized by different levels of production, and the resulting b-value is probably derived from a heterogeneous sample. For the smallest volume (0-4 km) the sample size does not allow to estimate b-value by vde21.

***b-value changes: Mapping*** - An alternative and less subjective approach to the radial analysis presented above is to map b-value on a dense spaced grid (1 km), selecting the events within a constant radius (5km), for the two significative time periods. Results are shown in Figure 5. For the first period, the lowest b-values (0.7-0.8) are found around the Huizinge epicentre, increasing with the distance, reaching values of about 1.2-1.3 in the outer parts. In the second period (2014-2022), the whole field exhibits more uniform values of about 0.8-0.9. Also in this case, the calculations have been performed by both AU66 (Figure 5 a-b) and vde21 estimator (Figure 5 c-d). These results are fully consistent with the radial sampling approach presented in Figure 3 and 4.

Maps of the differences in between the two periods are shown in Figure 6 (a, for AU66, and b, for vde21) are also consistent with the previous analysis. b-value generally increases in the North in period 2 and decrease in the South. For a direct comparison, I plot the FMDs in a 4-km radius around one grid node where the b-value remain constant (Figure 6c, grid node centred in the Huiginze epicentre) and two grid nodes with a marked decrease: one centred in the 2021 Ml 3.2 Garrelsweer event (Figure 6d, 4-km radius) and one in the South (Figure 6e, 5-km radius).

***b-value changes: Temporal analysis*** - A continuous time series analysis of b-values adds to the analysis by not making assumptions on the analysis periods. To compute b-values with time, because the magnitude of completeness varies over time, I used the vde21 approach and calculate uncertainty with bootstrapping, choosing a constant number of events' approach to have robust and comparable estimations. Following the approach by Tormann et al. (2013), a window containing 120 events results in a good combination of robustness and time resolution, the window is then moved through the catalogue event

by event. Note that because the values are plotted at the time of the last event in the subset, there will be independent estimates every 120 events; for the same reason, the largest variations are visible with a delay, the length of which will depend on the time interval required to have an independent sample. In this case, the expected variations after production changes in 2014, will be shifted to the right part of the graph.

Two areas are analyzed separately in Figure 7: North and South of 593000. b-values in the South (red line) are consistently higher, in line with the previous analysis. In addition, the values in the South are more variable: b-values in the southern increase from 2010 onwards, while the ones in the Northern part (blue line) slightly decrease. After 2015, the red line decreases sharply, continuing parallel but about 0.2 units higher than the blue line until about 2021 when the two lines currently converge toward a common value. As explained above, there is a delay in displaying changes due to the time length of the sample.

**b-value and compaction** - Bourne et al. (2014; from now on, B2014) analyzed the correlation between b-values and compaction in more detail, with the aim of forecasting future seismicity and hence seismic hazard and risk based on the expected future reservoir compaction. They first establish that 90% of the events with  $M_l \geq 1.5$  occurred at a time and place when the reservoir compaction was at least 0.18 implying that the occurrence of earthquakes, in space and time, is strongly influenced by the reservoir compaction. B2014 then directly compared compaction and b-value by applying an innovative sampling approach: each event in the catalogue was labelled according to the reservoir compaction at the event's time and epicentre. Then, subsets of at least 50 events

were selected within a range of compaction values and b-value estimates by AU66 and their 67% confidence intervals determined. The analysis indicated a statistically significant decrease in b-value with increasing compaction. The original figure by B2014 is shown here as inset in Figure 8a.

As a first step, I here reproduce and update the same plot for the same period (1991-2012; Figure 8a) used by B2024, and then analyse if the same correlation holds for the most recent data (2013-2022; Figure 8b) and for the entire catalogue (Figure 8c). I use a different compaction model (NAM, 2021) and a constant compaction interval ( $\pm 5$  cm) with respect to B2014, making the analysis more systematic: in the B2014 approach, subsets are not independent but strongly overlap with each other. The results in Figure 8 confirm the observations by B2014 for the period 1991 – 2012, and show that in the period 2013-2022, the dependence is even more pronounced, probably due to the improved quality and homogeneity of the available data with time. The FMDs of the maximum ( $b = 1.1$ ) and minimum b-values ( $b = 0.79$  and  $0.7$ ) for each time and compaction interval are also plotted in the frames d-f. The differences between the b-values are statistically highly significant, and the FMDs well adhere to a power law fit.

The B2014 approach samples events from all areas of the field, irrespective of location or time, destroying potential space-time information on the correlation of b-values and compaction. An alternative approach is to compare the compaction model, the seismicity and the b-value maps directly, using the same grid of the compaction data (0.5 km; Figure 9a). As noted by B2014, most induced earthquakes are concentrated in areas of higher compaction, and especially events with larger magnitudes, but there are also aseismic high compaction regions. Moreover, the very areas with the highest compaction values

are almost (dark red in the map). The epicentres of events at higher magnitudes seem to contour this central patch; the same aseismic patches were already evident in the Figure 9 in B2014: the absolute compaction values between the two models are different but the general trend is similar. The analysis confirms that earthquakes occur only in areas of high compaction values, but some areas of high compaction, are aseismic.

To quantitatively correlate b-value and compaction, I determine b-values on sub-samples composed by the events within a 5-km radius to each grid node, for the periods 1991-2012 and 2013-2022 (Figure 9 b-c). In the first period (Figure 9b), b-value spans from about 0.5 to 1.4 and no clear trend is visible in the compaction and b-value scatterplot. After 2013 (Figure 9c), b-values in the field are more homogeneous, limited to the range between 0.8 and 0.6; there is a weak anticorrelation between b-values and subsidence. In an additional comparison that considers the spatial seismicity at a given time, I first calculated the b-value for each event in the catalogue by selecting the 50 events closest to the origin time of the event; this value was then compared to the compaction value of the closest grid node at the origin time of the event: the results shown in Figure 9d do not show a correlation.

***b-values, magnitude and compaction rate*** - While b-values seem closely correlated to compaction, an alternative hypothesis to investigate now is that b-values correlate with compaction rate, thus strain rate, rather than absolute compaction or strain. Rate-dependence has been proposed also as a mechanism to explain seismicity rate but has not yet been correlated with b-values. To evaluate this correlation, differential compaction is computed at every earthquake time, averaging over the last 10 year of compaction values, and then b-values are computed for the nearest 50 events in space

391 prior to this time. The resulting clear correlation between b-values (y-axis) and  
392 compaction rate (x-axis) is shown in Figure 10a: b-values are lowest ( $b < 0.8$ ) if  
393 compaction rates are exceeding about 0.4 cm/year.

394  
395 Higher b-values then directly translate in a smaller chance of larger and potentially felt  
396 or damaging earthquakes. Figure 10b displays the correlation between compaction rates  
397 (x-axis), still in the last 10 years before the origin time, and the maximum observed  
398 magnitude (y-axis) in a 0.5-km cell centred on the compaction grid (NAM, 2021). Events  
399 above M2 occurred if the threshold of compaction rates of 0.28 cm/year is exceeded,  
400 events above M3 only once the compaction rates exceed 0.36 cm/year: the gray area in  
401 the upper left corner represents the magnitude-compaction-rate associations within  
402 which no seismicity is observed.

### 403 404 *Implications for seismic hazard*

405  
406 For the first 30 years of gas production, no seismicity was observed in the field, but the  
407 continuous extraction led to the progressive reactivation of normal faults, and seismicity  
408 eventually started, reaching the maximum magnitude of 3.6 in 2012. While the link  
409 between seismic activity rate and production is well studied and widely accepted within  
410 the community (e.g., Segall, 1992; Zoback, 2007), the evolution of the average size  
411 distribution, the b-value, and production parameters are much less studied and disputed.  
412 This study adds in several relevant ways to the conceptual understanding of the  
413 seismicity in Groningen, but also to other depletion related induced seismicity. In doing  
414 so, the study also contributes to improving seismic hazard and risk assessment and to  
415 risk management strategies.

416

417 Unravelling the space and time evolution of the b-value is challenging, especially in area  
418 of sparse data. In the Groningen area, only 1487 induced earthquakes have been located  
419 so far since 1991, and only 637 above the estimate overall magnitude of completeness  
420 (Dost et al., 2017; Paleja and Bierman, 2016). This dataset is small, severely limiting the  
421 ability to resolve spatial and temporal patterns. This task is further complicated by the  
422 threat of biases in magnitudes, and by heterogeneity in magnitude reporting with space  
423 and time (e.g., Gulia et al., 2012; Tormann et al., 2010). The biggest challenging, however,  
424 is not data but process related: the stressing path these faults more than 1500 known  
425 (and countless more unknown) undergo is strongly depending on production  
426 parameters, which are variable with space and time. If indeed b-values are depending on  
427 the applied differential stresses as suggested from numerous studies (e.g., Schorlemmer  
428 et al., 2005), then one should expect a temporal and spatial evolution of b-values in the  
429 field. Even more complexity is added considering that the evolution of the shear stress on  
430 normal faults during compartmentalized depletion is non-linear if one also accounts for  
431 stress-dependent permeability and linear poroelasticity (Zbinden et al., 2017).

432

433 And indeed, the first contribution of this study is to establish firmly that such a pattern  
434 does exist and is well explained by theory. The b-values are lowest in the areas of highest  
435 compaction (Figure 3 and 4), and they change with time: increasing compaction in the  
436 Southern part of the field due to changes in the production pattern leads to decreases in  
437 b-values in these areas. I established these key findings using three different analysis  
438 approaches: concentric volumes focussed on the 2012 event hypocentre (Figures 3 and  
439 4), spatial maps and differential b-value maps (Figures 5 and 6) and time-series analysis  
440 (Figure 7). I also use two different approaches to estimate b-values: AU66 and vde21.

Each mapping and method offer distinct advantages but also limitations, but the fact that all lead to broadly the same results strongly supports for the overall interpretation that b-values in the Groningen area are variable with space and time in a systematic and explainable way. These findings, obtained through the combined analysis of space and time as a function of production (field history in Figure 1), solidify and extend previous studies (Wentinck, 2015; Bourne and Oates, 2015; Muntendam-Bos et al., 2017). Note that method of van der Elst (2021) to estimate b-value has proven to be comparable, if not superior as an analysis tool.

The hazard implication of variable b-values is substantial: the probability of having an M 5 or larger in an area with a low b-value is thousands of times more than the probability of having the same event in an area with a high b-value. Of course, beside the b-value, the activity rate (a-value) needs to be estimated and considered also.

The change in differential stress that a steeply oriented boundary fault undergoes during 50 years of production is quite substantial, as demonstrated for example by Zbinden et al. (2017). Differential stresses at reservoir depth increase from about 19.6 Mpa to value of 30.6 Mpa (base case) to 36 Mpa (case with multiple wells). The b-value changes of this doubling of differential stresses can be compared to past studies: Goertz-Allmann and Wiemer (2012) derived a b-value dependence on differential stress ( $S_d$ ) for the Basel induced seismicity of  $b = -0.022 * S_d$ , with a change in differential stress of 10 – 16 Mpa, we expect a decrease of the b-value of 0.22 to 0.35, comparable the observed range in this study. The b-value dependence on depth results in similar values (Spada et al., 2013; Scholz, 2015; Petrucci et al., 2019), with observation showing that a doubling of the depth will reduce the b-value of crustal earthquakes on average by 0.2. Laboratory

studies are likewise in line with these observations: Goebel et al. (2013) for example report that a b-value change of about 0.3 – 0.4 is observed when progressing from 60% to 100% of the maximum strength of a fault. Therefore, the temporal and spatial changes observed here are well in line with the contemporary understanding of b-value. Given that hydro-geomechanical reservoir models of the Groningen area exist (van Wees et al., 2018; Bourne and Oates, 2017), it seems feasible to build models that are recreating the observations and using them to forecast future seismicity beyond empirical correlations.

One of the most striking results of this study is the very clear correlation of b-value and compaction, or compaction rate (Figure 9 and 10). B2014 had already proposed the inverse correlation between b-value and compaction in the field, here I confirm the findings by B2014 and extend the same analysis to 2022. Although I adopted a different, more updated compaction model from B2014, the observed correlations in the earlier period are in good agreement. More importantly, the correlation is maintained with the higher quality, recent data (Figure 8b). This striking correlation represents a major gradient in b-value, equal to the ones with depth (Spada et al., 2013), focal mechanism (Schorlemmer et al, 2005), mainshocks (Gulia et al., 2018) or pore pressure (Goertz-Allmann and Wiemer, 2013). All of these represent major gradients of differential stress in the Earth and are well explained in an ever more refined framework of b-value and differential stress correlations.

However, it is unclear (but important) at this point what exactly is responsible for the change in b-values, or what the best predictor of b-value evolution is: absolute compaction, compaction rate (so the temporal derivative of compaction at on place), or maybe compaction gradient (the spatial derivative of the compaction). Figures 9 and 10

suggest that all three are potential candidates, and of course all are related. The data are currently not able to distinguish between these hypotheses, but Figure 10b hints that compaction rates play a more important role in limiting larger magnitudes than absolute compaction: events with  $M > 2$  occur also at low absolute compaction (blue dots) but not at low compaction rates.

The fact that now the b-value in the North and in the South are now both equal and generally low is in terms of hazard perspective not ideal: switching production to the South has brought temporally relieve, by decreasing the rate of seismicity in the Loppersum area temporarily (Muntendam-Bos, 2020) and by increasing seismicity in an area of high b-value. But now the b-values in the South are equally low and continued production in any part of the field is likely to lower them further, suggesting that the seismic risk will continue to be substantial if production continues. I can only speculate that once production stops, b-value will also gradually increase as the stresses in the field are equalised.

In terms of risk mitigation strategies, the results presented in this study, when also combined with related models that forecast the seismicity, offer one potential avenue for continued exploitation of the field. The seismic risk is substantially lower while b-values are high, so Figure 9 and B2014 suggests that absolute compaction at any location should remain below 10 – 15 cm. This would also imply low seismicity rates but does not allow to produce any further in a majority of the field. If instead as suggested from this analysis shown in Figure 10b compaction rate is the driving mechanism, then a possible strategy would be to produce slowly and essentially everywhere, but not exceeding values of 0.2 – 0.3 cm of compaction per year. To better resolve this highly important issue that may allow continue production of gas in times of dire need, I suggest that an analysis of the

seismicity data based on a template-matched catalogue with a lower magnitude completeness, combined with geo-mechanical modelling of the stress dependent b-value may allow to add further support to the new idea of compaction rate driven b-values.

## ***Data and Resources***

Geomechanical, seismological, and geodetic data pertaining to the Groningen gas field: a data package used in the "Mmax II Workshop", on constraining the maximum earthquake magnitude in the Groningen field are available at <https://public.yoda.uu.nl/geo/UU01/RHHRPY.html>, DOI: 10.24416/UU01-RHHRPY

## ***Acknowledgements***

I gratefully acknowledge Jan van Elk, the Nederlandse Aardolie Maatschappij (NAM) and Julian Bommer for the Second Workshop on Mmax for Seismic Hazard and Risk Analysis in the Groningen Gas Field, Amsterdam, 13-17 June 2022 and for their support. I thank Onno van Wal and Stephen Bourne (Shell Global Solutions International B.V) for sharing data and Paolo Gasperini and Gianfranco Vannucci for their feedback on the manuscript. This study also benefits from the always stimulating discussions with Stefan Wiemer, especially on the correlation between b-value and compaction rates.

## **References**

Aki, K. (1965). Maximum likelihood estimate of b in the formula  $\log N = a - bM$  and its confidence limits, *Bull. Earthq. Res. Inst. Univ. Tokyo* 43, 237–239.

540

541 Bachmann, C., S. Wiemer, B. P. Goertz-Allmann, and J. Woessner (2012). Influence of pore-  
542 pressure on the event-size distribution of induced earthquakes, *Geophys. Res. Lett.* 39, no.  
543 9, L09302, doi: 10.1029/2012GL051480.

544 Bommer, J.J. and J. van Elk (2017). Comment on “The Maximum Possible and the  
545 Maximum Expected Earthquake Magnitude for Production - Induced Earthquakes at the  
546 Gas Field in Groningen, The Netherlands” by Gert Zöller and Matthias  
547 Holschneider. *Bull. Seism. Soc. Am.*; 107, no. 3: 1564–1567.  
548 doi: <https://doi.org/10.1785/0120170040>

549 Bourne, S. J., Oates S. J. (2017). Development of statistical geomechanical models for  
550 forecasting seismicity induced by gas production from the Groningen field, *Neth. J. Geosci*  
551 (96): s175-s182

552 Bourne, S. J., S. J. Oates, J. van Elk, and D. Doornhof (2014). A seismological model for  
553 earthquakes induced by fluid extraction from a subsurface reservoir, *J. Geophys. Res. Solid*  
554 *Earth*, 119, doi:10.1002/2014JB011663.

555 Cornell, C. A. (1968). Engineering seismic risk analysis, *Bull. Seismol. Soc. Am.* 58, no. 5,  
556 1583–1606.

557 De Jager, J., and Visser, C. (2017). Geology of the Groningen field – an  
558 overview. *Netherlands Neth. J. Geosci*, 96, no. 5, S3-S15. doi:10.1017/njg.2017.22

559 Dost, B., Goutbeek, F., Eck, T.V. and Kraaijpoel, D. (2012). Monitoring induced seismicity  
560 in the North of the Netherlands: status report 2010, *Tech. Rep.*, Koninklijk Nederlands  
561 Meteorologisch, de Bilt, The Netherlands.

562

563 Dost, B., and J. Spetzler (2015). Probabilistic seismic hazard analysis for induced  
564 earthquakes in Groningen. KNMI report. Royal Netherlands Meteorological Institute (De  
565 Bilt), 13.

566

567 Dost, B., E. Ruigrok, and J. Spetzler (2017). Development of probabilistic hazard  
568 assessment for the Groningen gas field, *Neth. J. Geosci.*, **96**, s235–s245.

569 Goebel, T. H. W., D. Schorlemmer, T. W. Becker, G. Dresen, and C. G. Sammis (2013).  
570 Acoustic emissions document stress changes over many seismic cycles in stick-slip  
571 experiments, *Geophys. Res. Lett.* 40, 2049–2054, doi: 10.1002/grl.50507.

572 Goertz-Allmann, B.P. and S. Wiemer (2013). Geomechanical modeling of induced  
573 seismicity source parameters and implications for seismic hazard assessment. *Geophys.*;  
574 78, no. 1: KS25–KS39. doi: <https://doi.org/10.1190/geo2012-0102.1>

575 Gulia, L., P. Gasperini and S. Wiemer (2022). Comment on “High - Definition Mapping of  
576 the Gutenberg-Richter  $b$  - Value and Its Relevance: A Case Study in Italy” by M. Taroni, J.  
577 Zhuang, and W. Marzocchi. *Seism. Res. Lett.*, 93, no. 2A: 1089–1094.  
578 doi: <https://doi.org/10.1785/0220210159>.

579

Gulia, L. and S. Wiemer (2021). Comment on “Two Foreshock Sequences Post Gulia and Wiemer (2019)” by Kelian Dascher - Cousineau, Thorne Lay, and Emily E. Brodsky. *Seism. Res. Lett.*, 92, no. 5: 3251–3258. doi: <https://doi.org/10.1785/0220200428>.

Gulia, L., S. Wiemer, G. Vannucci (2020). Pseudoprospective Evaluation of the Foreshock Traffic-Light System in Ridgecrest and Implications for Aftershock Hazard Assessment, *Seismol. Res. Lett.* 91, no. 5, 2828–2842. doi: <https://doi.org/10.1785/0220190307>

Gulia, L., and S. Wiemer (2019). Real-time discrimination of earthquake foreshocks and aftershocks, *Nature* 574, 193–199.

Gulia, L., Rinaldi, A.P., Tormann, T., Vannucci, G., Enescu, B., and S. Wiemer (2018). The effect of a mainshock on the size distribution of the aftershocks, *Geophys. Res. Lett.* 45, doi: 10.1029/2018GL080619.

Gulia, L., Tormann, T., Wiemer, S., Herrmann, M., and S. Seif (2016). Short-term probabilistic earthquake risk assessment considering time dependent b values. *Geophys. Res. Lett.*, 43, 1100–1108. <https://doi.org/10.1002/2015GL066686>

Gulia, L., S. Wiemer, and M. Wyss (2012). Catalog artifacts and quality controls, community online resource for statistical seismicity analysis, doi: 10.5078/corssa-93722864.

603 Gulia, L., and S. Wiemer (2010). The influence of tectonic regimes on the earthquake size  
604 distribution: A case study for Italy. *Geophys. Res. Lett.*, 37, L10305.  
605 <https://doi.org/10.1029/2010GL043066>  
606

607 Gutenberg, B., and C.F. Richter (1944). Frequency of earthquakes in California. *Bull.*  
608 *Seismol. Soc. Am.*, 34, 185–188  
609

610 Harris, C.K., and S. Bourne (2015). Maximum Likelihood Estimates of b-Value for Induced  
611 Seismicity in the Groningen Field, Restricted Draft Report,  
612 [https://www.sodm.nl/documenten/publicaties/2015/06/23/6.-maximum-likelihood-](https://www.sodm.nl/documenten/publicaties/2015/06/23/6.-maximum-likelihood-estimates-of-b-value-for-induced-seismicity-in-the-groningen-field-c.k.-harris--s.j.-bourne-restricted-draft-report-1-mei-2015)  
613 [estimates-of-b-value-for-induced-seismicity-in-the-groningen-field-c.k.-harris--s.j.-](https://www.sodm.nl/documenten/publicaties/2015/06/23/6.-maximum-likelihood-estimates-of-b-value-for-induced-seismicity-in-the-groningen-field-c.k.-harris--s.j.-bourne-restricted-draft-report-1-mei-2015)  
614 [bourne-restricted-draft-report-1-mei-2015.](https://www.sodm.nl/documenten/publicaties/2015/06/23/6.-maximum-likelihood-estimates-of-b-value-for-induced-seismicity-in-the-groningen-field-c.k.-harris--s.j.-bourne-restricted-draft-report-1-mei-2015)  
615

616 Hol, S., A., van der Linden, S., Bierman, S. Marcelis, A. Makurat (2018). Rock Physical  
617 Controls on Production-induced Compaction in the Groningen Field. *Sci. Rep.*, 8, 7156.  
618 <https://doi.org/10.1038/s41598-018-25455-z>  
619

620 Ishimoto, M., and K. Iida (1939). Observations sur les séismes enregistrés par le  
621 microséismographe construit dernièrement, *Bull. Earthq. Res. Inst.* 17, 443–478 (in  
622 French).  
623

624 Mehranpour, M. H., Hangx, S. J. T., and C.J. Spiers (2021). Compaction of the Groningen gas  
625 reservoir sandstone: Discrete element modeling using microphysically based grain- scale  
626 interaction laws. *J. Geophys. Res.: Solid Earth*, 126, e2021JB021722. [https://doi.](https://doi.org/10.1029/2021JB021722)  
627 [org/10.1029/2021JB021722](https://doi.org/10.1029/2021JB021722)

628

629 Muntendam-Bos, A.G., and N. Grobbe (2022). Data-driven spatiotemporal assessment of  
630 the event-size distribution of the Groningen extraction-induced seismicity catalogue. *Sci.*  
631 *Rep.*, 12, 10119 (2022). <https://doi.org/10.1038/s41598-022-14451-z>

632

633 Muntendam-Bos, A.G. (2020) Clustering characteristics of gas-extraction induced  
634 seismicity in the Groningen gas field, *Geophys. J. Int.*, 221, no. 2, 879–  
635 892, <https://doi.org/10.1093/gji/ggaa038>

636

637 Muntendam-Bos, A.G., Roest, J.P.A. and H.A. de Waal (2017). The effect of imposed  
638 production measures on gas extraction induced seismic risk. In: *Netherlands J. Geosc.*  
639 96.5, s271–S278.

640

641 Muntendam-Bos, A.G., and J.A. de Waal (2013). Reassessment of the probability of higher  
642 magnitude earthquakes in the Groningen gas field. SodM (National Mines Inspectorate)  
643 report: 33 pp. Open access via  
644 [https://www.rijksoverheid.nl/documenten/rapporten/2013/01/16/](https://www.rijksoverheid.nl/documenten/rapporten/2013/01/16/reassessment-of-the-probability-of-higher-magnitude-earthquakes-in-the-groningen-gas-field)  
645 [reassessment-of-the-probability-of-higher-magnitude-earthquakes-in-the-groningen-](https://www.rijksoverheid.nl/documenten/rapporten/2013/01/16/reassessment-of-the-probability-of-higher-magnitude-earthquakes-in-the-groningen-gas-field)  
646 [gas-field.](https://www.rijksoverheid.nl/documenten/rapporten/2013/01/16/reassessment-of-the-probability-of-higher-magnitude-earthquakes-in-the-groningen-gas-field)

647

648 NAM (2016). Winningsplan Groningen Gasveld 2016. Nederlandse Aardolie Maatschappij  
649 BV (Assen). Available at [www.nam.nl/feiten-en-cijfers/gaswinning.html](http://www.nam.nl/feiten-en-cijfers/gaswinning.html).

650

NAM (2021). Groningen long term subsidence forecast, EP202008201822, <https://nam-onderzoeksrapporten.data-app.nl/reports/download/groningen/en/d8970d78-f51a-4a3b-85d4-f80f42d055af>

Paleja, R., Bierman, S. and M. Jones (2016). Impact of production shut-in on interevent time in Groningen. A statistical perspective. Shell report. Royal Dutch Shell (The Hague): 35pp. Available at [www.nam.nl/feiten-en-cijfers](http://www.nam.nl/feiten-en-cijfers).

Papadopoulos, G. A., Charalampakis, M., Fokaefs, A., and G. Minadakis, (2010). Strong foreshock signal preceding the L'Aquila (Italy) earthquake (Mw 6.3) of 6 April 2009. *Nat. Hazards Earth Syst. Sc.*, 10, no. 1, 19–24. <https://doi.org/10.5194/nhess-10-19-2010>

Petrillo, G., Lippiello, E., Landes, F.P., A. Rosso (2020). The influence of the brittle-ductile transition zone on aftershock and foreshock occurrence. *Nat. Commun.* 11, 3010. <https://doi.org/10.1038/s41467-020-16811-7>

Petrucelli, A., P. Gasperini, T. Tormann, D. Schorlemmer, A. P. Rinaldi, G. Vannucci, and S. Wiemer (2019). Simultaneous dependence of the earthquake-size distribution on faulting style and depth, *Geophys. Res. Lett.* 46, no. 20, 11044–11053, doi: 10.1029/2019GL083997

Segall, P. (1992). Induced stresses due to fluid extraction from axisymmetric reservoirs. *Pure Appl. Geophys.*, 139, no. 3/4: 535–560.

675 Scholz, C. H. (1968). The frequency-magnitude relation of microfracturing in rock and its  
676 relation to earthquakes, *Bull. Seismol. Soc. Am.* 58, 399–415.  
677

678 Scholz, C.H. (2015). On the stress dependence of the earthquake b value, *Geophys. Res.*  
679 *Lett.*, 42, 1399–1402, doi: 10.1002/2014GL062863.  
680

681 Schorlemmer D., S. Wiemer and M. Wyss (2005). Variations in earthquake-size  
682 distribution across different stress regimes. *Nature*, 437(7058), 539–542.  
683 <https://doi.org/10.1038/nature04094>  
684

685 Shi, Y., and B. Bolt (1982). The standard error of the magnitude frequency b value, *Bull.*  
686 *Seismol. Soc. Am.* 72, no. 5, 1677–1687.  
687

688 Smith, J. D., Avouac, J.-P., White, R. S., Copley, A., Gualandi, A., and S. Bourne (2019).  
689 Reconciling the long-term relationship between reservoir pore pressure depletion and  
690 compaction in the Groningen region. *J. Geophys. Res.: Solid Earth*, 124, 6165–6178.  
691 <https://doi.org/10.1029/2018JB016801>  
692

693 Spada, M., Tormann, T., Wiemer, S., and B. Enescu (2013). Generic dependence of the  
694 frequency-size distribution of earthquakes on depth and its relation to the strength  
695 profile of the crust. *Geophys. Res. Lett.*, 40, no. 4, 709–714.  
696 <https://doi.org/10.1029/2012GL054198>

697 Tormann, T., S. Wiemer, A. Mignan (2014). Systematic survey of high-resolution b value  
698 imaging along Californian faults: Inference on asperities, *J. Geophys. Res.*, 119, no. 3, 2029-  
699 2054, <https://doi.org/10.1002/2013JB010867>

700 Tormann, T., Enescu, B., Woessner, J. and S. Wiemer (2015). Randomness of megathrust  
701 earthquakes implied by rapid stress recovery after the Japan earthquake. *Nat. Geosci.* 8,  
702 152–158.

703

704 Tormann T., S. Wiemer, and E. Hauksson (2010), changes in reporting Rates in the  
705 Southern California Earthquake Catalog, Introduced by a New Definition of Ml, *Bull. Seism.*  
706 *Soc. Am.* 100, no. 4, 1733{1742

707

708 Utsu, T. (1966). A statistical significance test of the difference in b-value between two  
709 earthquake groups, *J. Phys. Earth*, 14, 34-40.

710

711 van der Elst, N. J. (2021). B-positive: A robust estimator of aftershock magnitude  
712 distribution in transiently incomplete catalogs. *J. Geophys. Res.: Solid Earth*, 126,  
713 e2020JB021027. <https://doi.org/10.1029/2020JB021027>

714

715 Van Elk, J., Bourne, S. J., Oates, S.J., Bommer, J.J., Pinho, R. and H. Crownley (2019). A  
716 Probabilistic Model to Evaluate Options for Mitigating Induced Seismic Risk. *Earthq.*  
717 *Spectra*, 35, no. 2, 537-564. doi:10.1193/050918EQS118M

718

van Thienen-Visser, K., and J. N. Breunese (2015). Induced seismicity of the Groningen gas field: History and recent developments: *Lead. Edge*, 34, 664–671, doi: 10.1190/tle34060664.1.

Van Thienen-Visser, K., and P. Fokker (2017). The future of subsidence modelling: Compaction and subsidence due to gas depletion of the Groningen gas field in the Netherlands. *Neth. J. Geosci.*, 96, no. 5, S105-S116. doi:10.1017/njg.2017.10

van Wees, J.D., S. Osinga, K. van Thienen-Visser, P. A Fokker (2018). Reservoir creep and induced seismicity: inferences from geomechanical modeling of gas depletion in the Groningen field, *Geophys. J. Int.*, 212, no. 3, 1487–1497, <https://doi.org/10.1093/gji/ggx452>

Wentinck, H.M. (2015), Induced seismicity in the Groningen field - statistical assessment of tremors along faults in a compacting reservoir, Shell Global Solutions International B.V., Rijswijk, Internal Report, 183 pp.

Willacy, C. van Dedem E., Minisini S., Li J., Blockland J.W., Das I. and A. Droujinine (2017). Full-waveform event location and moment tensor inversion for induced seismicity. *Geophys.*, 84, no. 2, KS39–KS47. <https://doi.org/10.1190/GEO2018-0212.1>.

Zbinden, D., A. P. Rinaldi, L. Urpi, and S. Wiemer (2017). On the physics-based processes behind production-induced seismicity in natural gas fields, *J. Geophys. Res. Solid Earth*, 122, 3792–3812, doi:10.1002/2017JB014003.

Zoback, M. D. (2007). Reservoir geomechanics: Cambridge University Press.  
<https://doi.org/10.1017/CBO9780511586477>

***Author's mailing address***

laura.gulia@unibo.it

***List of Figures and Captions***

Figure 1 –***Field history***: essential steps and significant time-intervals in the Groningen gas field since the start in gas production. Note that time is not scaled.

Figure 2 – ***Expected b-values*** - Theoretical and expected b-value in the field for two significant time periods according to the current literature on b-value: on the left) the lowest b-value are expected in the central part of the field, surrounded by higher values during the period of high production; on the right) decreasing b-values are expected in the outer part of the field due to the shift in production started in 2014.

Figure 3 –***b-value in doughnut-shaped spherical volumes*** - a) Seismicity in the field colored according to the distance from the epicentre of the 2012 Ml 3.6 event in Huizinge; b-c: frequency-magnitude distributions of the 4 volumes in frame (a) for the two periods under examination: before 2014 (b) and after (c). In the first period, the b-value increases with the distance from the Huizinge epicentre; in the second period, the values are more homogeneous.

767

768 Figure 4 – **Observed b-values** - a-b) b-value in spherical volumes from the epicentre of  
769 the 2012 Ml 3.6 event in Huizinge: in the period 1991-2014, the b-value increases with  
770 the distance (a); after 2014, the b-value is more homogeneous, tending to a common  
771 value (b); c-d) comparison between the b-value estimated by AU66 (blu dots; uncertainty  
772 by Shi and Bolt, 1982) and the ones calculated on the same dataset by vde21 (red dots,  
773 uncertainty by bootstrapping) before 2014 (c) and after (d).

774

775 Figure 5 – **Spatial evolution of b-value in time** - b-value maps for the periods 1991-2013  
776 and 2014-2022; a,b) maps calculated by AU66 and Mc from Dost et al. (2018) and Paleja  
777 and Bierman (2016); c-d) by vde21. The epicentres of the biggest events in the two  
778 periods are also shown.

779

780 Figure 6 – **FMDs in significative volumes** - a) maps of the differences between the two b-  
781 value maps in Figure 6 a-b; b) maps of the differences between the two b-value maps in  
782 Figure 6 c-d; c-e) comparison between the frequency-magnitude distributions of the b-  
783 value by AU66 for 3 locations (Huiginze, Garrelsweer and a grid node in the South, black  
784 dot in maps a-b) in the time periods 1991-2013 and 2014-2022.

785

786 Figure 7 – **b-value time-series** - b-value time-series for all the events North of 593000  
787 (blue line) and South of 593000 (red line) estimated by vde21, uncertainty by bootstrap  
788 (shaded colors). The two lines currently seems to converge toward a common value. The  
789 most important steps of the field history shown in Figure 1 are marked on the x-axis.

790

Figure 8 – ***b-value and compaction*** - a-c) b-value estimated by AU66 following B2014 on subsets of at least 50 events within the range  $\pm 5$  cm of compaction values, for the periods 1991-2012 (a), 2013-2022 (b) and for the entire period (1991-2022, c). The original figure 14 by B2014 is shown as inset in a.

d-f) comparison between the frequency-magnitude distributions of the minimum and maximum b-value for the same periods.

Figure 9 – ***Compaction map and b-value*** - a) compaction map: cumulative compaction at the year 2022, calibrated on the V6 scenario, operational strategy 2 (OS2; NAM 2021) on a grid of 0.5 km with superimposed seismicity from 1991 to May 2022; b-c) b-value versus compaction for the same 0.5-km spaced grid for the periods 1991-2012 and 2013-2022. Vertical bar: uncertainty by Shi and Bolt (1982); d) b-value calculated for each event in the catalog sampling the closest 50 event above  $M_c$  at the origin time versus the compaction of the closest grid node. Vertical bar: uncertainty by Shi and Bolt (1982).

Figure 10 – ***b-value, magnitude, and compaction rates*** - a) Correlation between b-value and compaction rates, expressed by the difference in compaction in 10 years before the event's origin time. Vertical bar: uncertainty by Shi and Bolt (1982); black solid line: linear regression modelling the relationship between b-value and difference in compaction ( $b = -0.0424x + 1.067$ ); b) correlation between the maximum magnitude for each 0.5 km cell and compaction rates, expressed by the difference in compaction in 10 years before the event's origin time, color-coded with respect to the absolute compaction. Gray area: if production does not result in the exceedance of about 0.35 cm of compaction per year, events above  $M_3$  do not occur.

*Figures with captions*

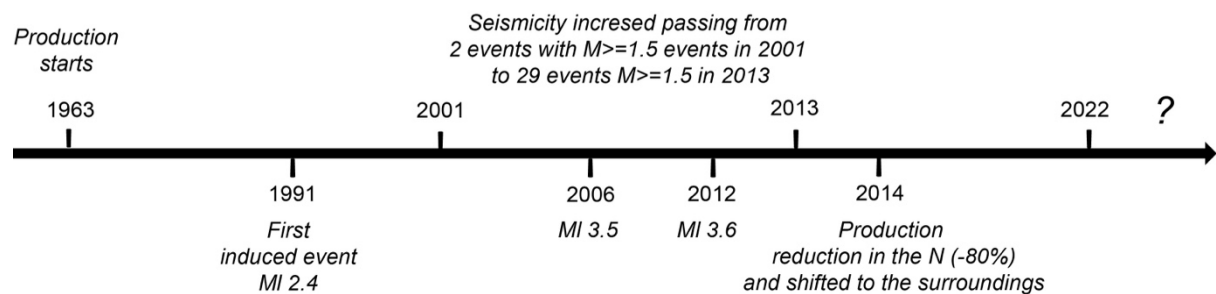
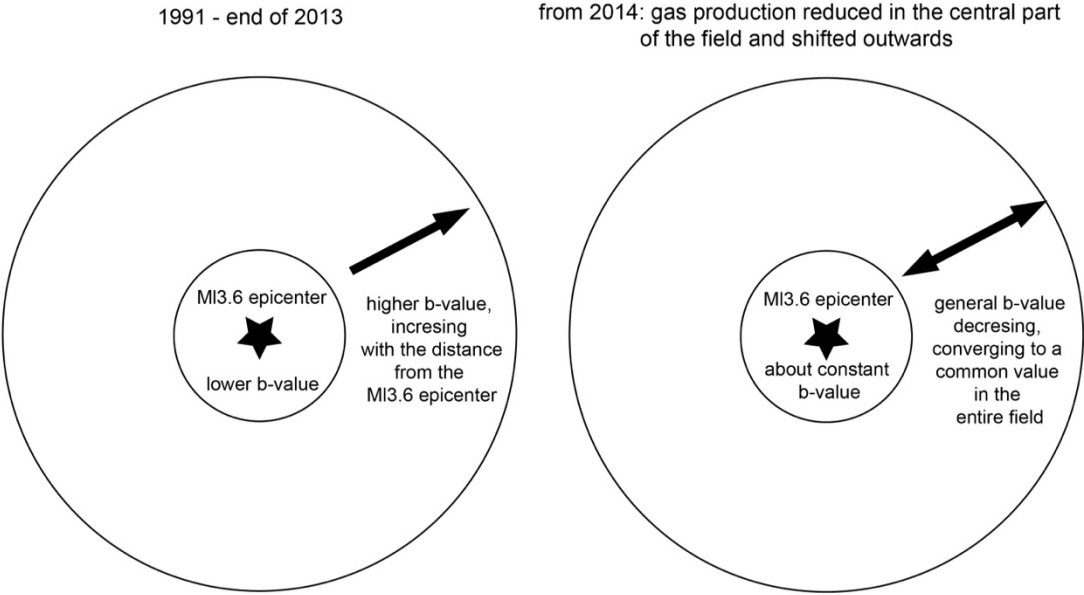


Figure 1 –**Field history**: essential steps and significant time-intervals in the Groningen gas field since the start in gas production. Note that time is not scaled.

Theoretical b-value evolution as a proxy of the state of the stress in the gas field



829

830

831 Figure 2 – **Expected b-values** - Theoretical and expected b-value in the field for two  
832 significant time periods according to the current literature on b-value: on the left) the  
833 lowest b-value are expected in the central part of the field, surrounded by higher values  
834 during the period of high production; on the right) decreasing b-values are expected in  
835 the outer part of the field due to the shift in production started in 2014.

836

### b-value in spherical volumes around the 2012 Huizinge event

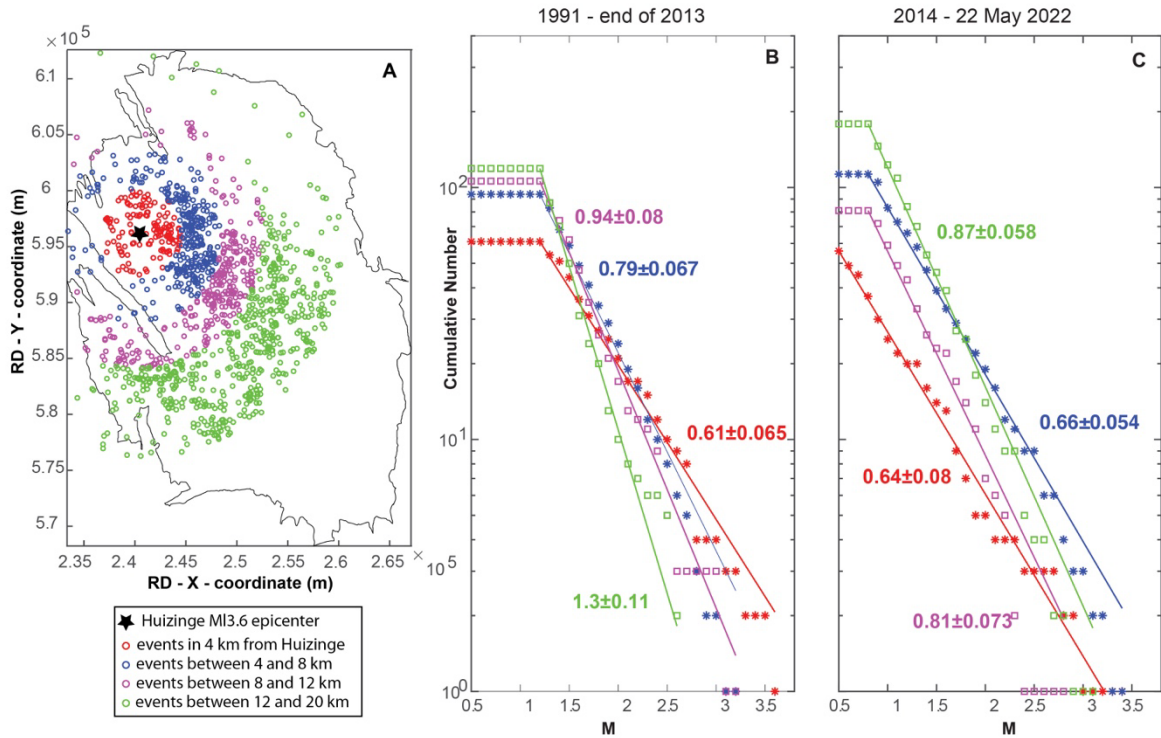
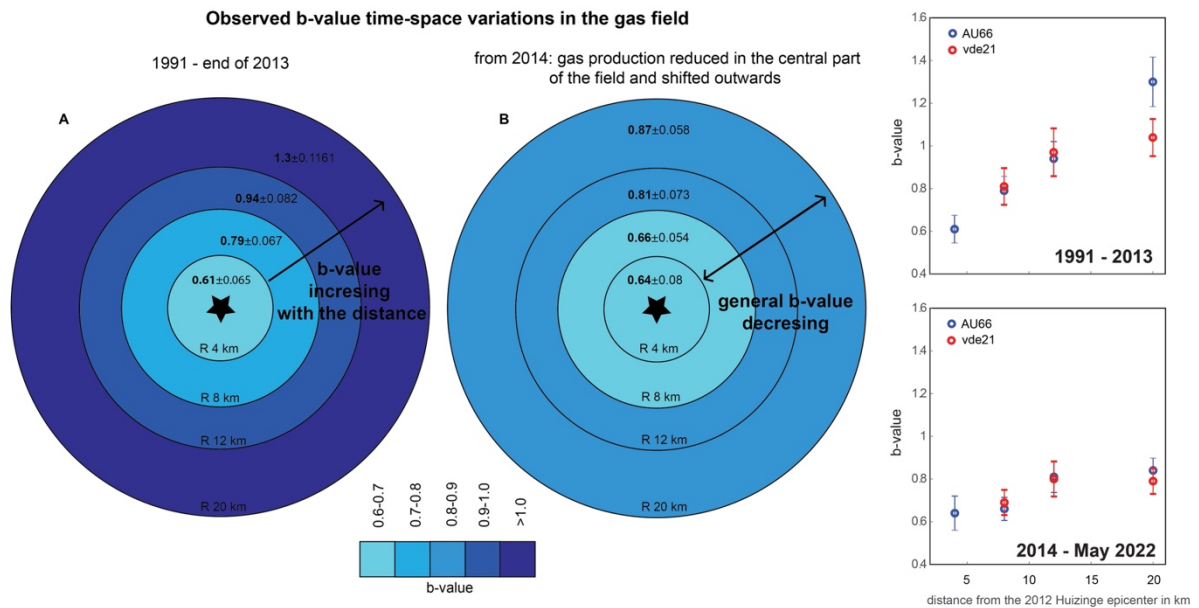


Figure 3 –*b-value in doughnut-shaped spherical volumes* - a) Seismicity in the field colored according to the distance from the epicentre of the 2012 Ml 3.6 event in Huizinge; b-c: frequency-magnitude distributions of the 4 volumes in frame (a) for the two periods under examination: before 2014 (b) and after (c). In the first period, the b-value increases with the distance from the Huiginze epicentre; in the second period, the values are more homogeneous.



846

847 Figure 4 – **Observed b-values** - a-b) b-value in spherical volumes from the epicentre of

848 the 2012 Ml 3.6 event in Huizinge: in the period 1991-2014, the b-value increases with

849 the distance (a); after 2014, the b-value is more homogeneous, tending to a common

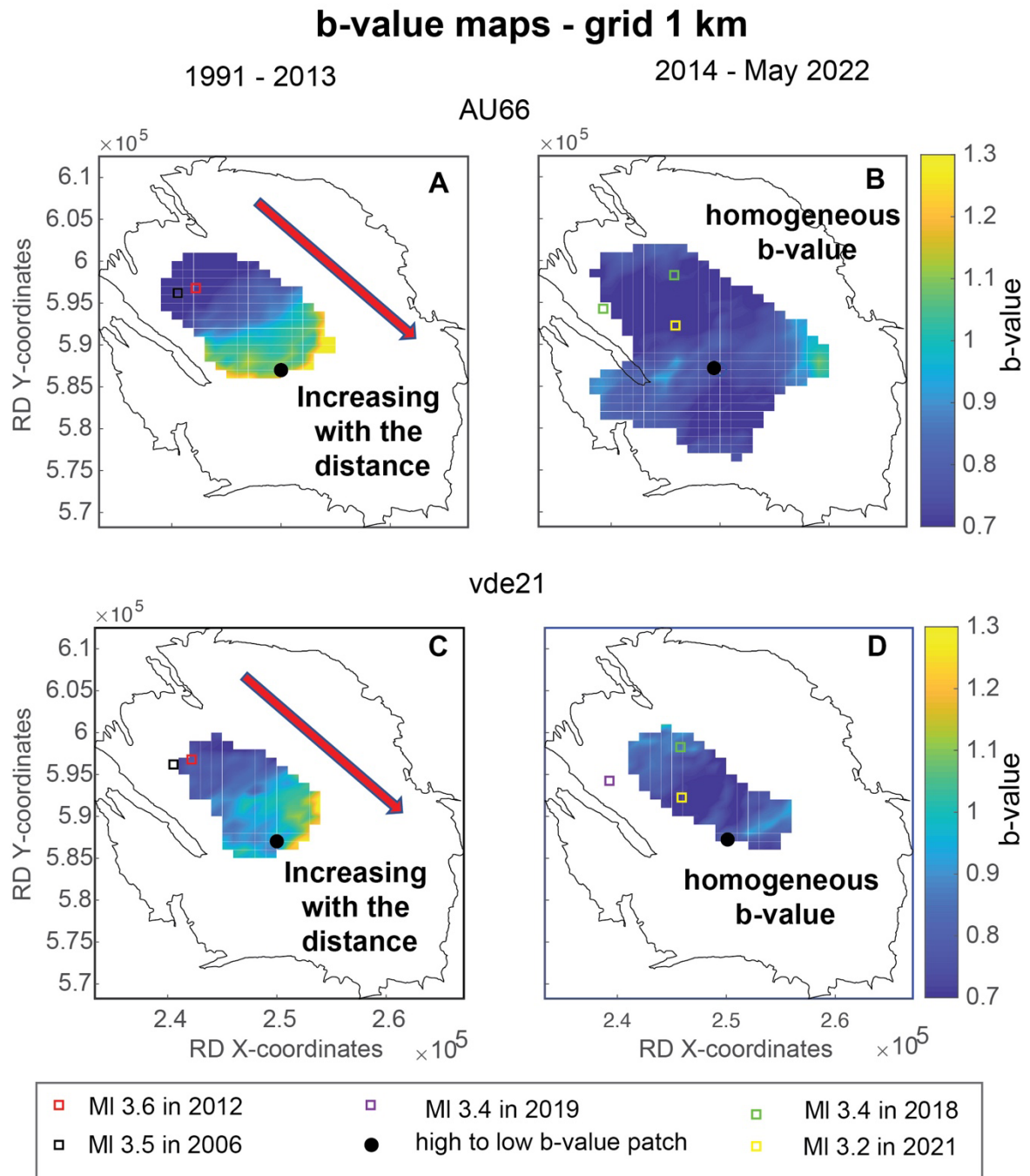
850 value (b); c-d) comparison between the b-value estimated by AU66 (blu dots; uncertainty

851 by Shi and Bolt, 1982) and the ones calculated on the same dataset by vde21 (red dots,

852 uncertainty by bootstrapping) before 2014 (c) and after (d).

853

854



855

856 Figure 5 – ***Spatial evolution of b-value in time*** - b-value maps for the periods 1991-2013  
857 and 2014-2022; a,b) maps calculated by AU66 and Mc from Dost et al. (2018) and Paleja  
858 and Bierman (2016); c-d) by vde21. The epicentres of the biggest events in the two  
859 periods are also shown.

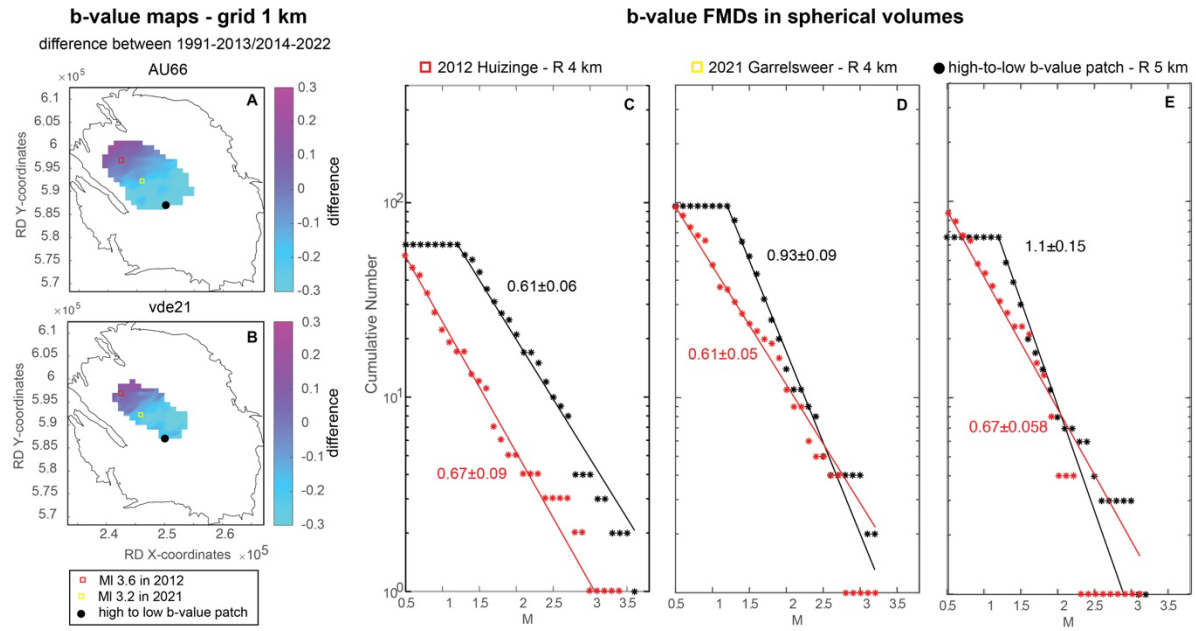
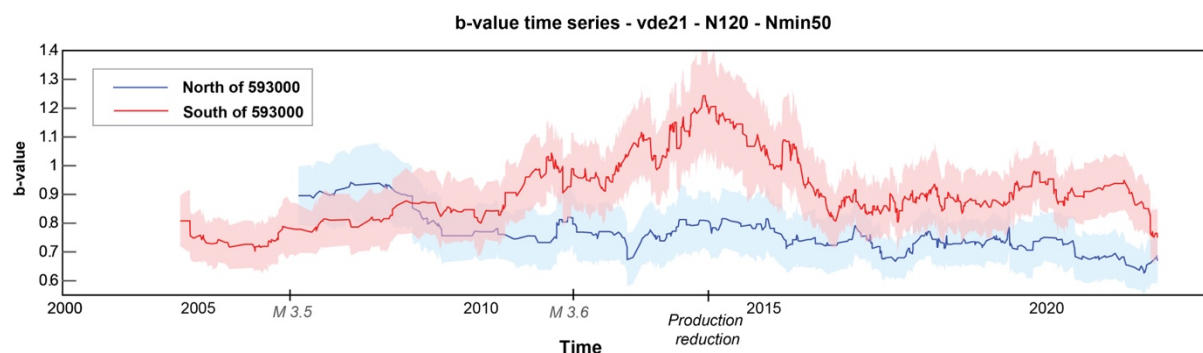


Figure 6 – *FMDs in significant volumes* - a) maps of the differences between the two b-value maps in Figure 6 a-b; b) maps of the differences between the two b-value maps in Figure 6 c-d; c-e) comparison between the frequency-magnitude distributions of the b-value by AU66 for 3 locations (Huiginze, Garrelsweer and a grid node in the South, black dot in maps a-b) in the time periods 1991-2013 and 2014-2022.

867

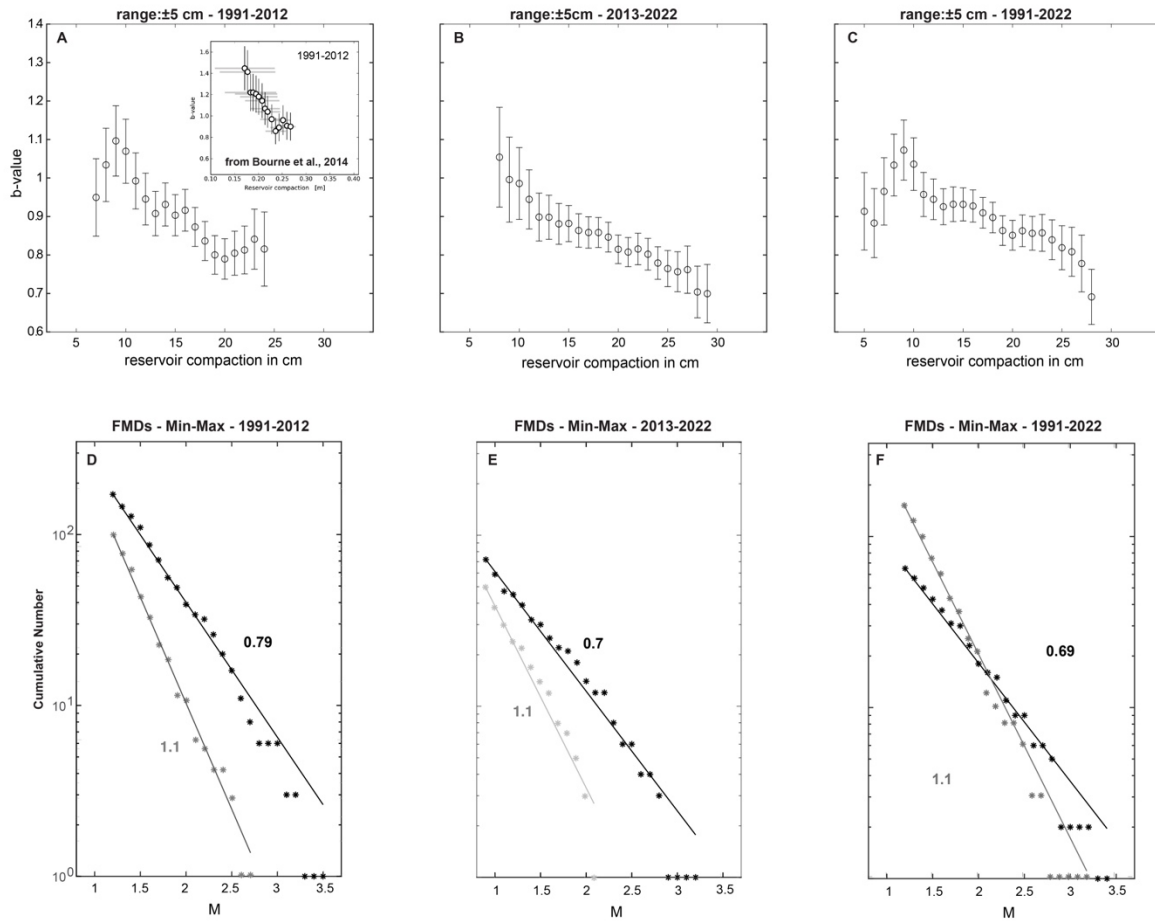


868

869

870 Figure 7 – ***b-value time-series*** - b-value time-series for all the events North of 593000  
871 (blue line) and South of 593000 (red line) estimated by vde21, uncertainty by bootstrap  
872 (shaded colors). The two lines currently seems to converge toward a common value. The  
873 most important steps of the field history shown in Figure 1 are marked on the x-axis.

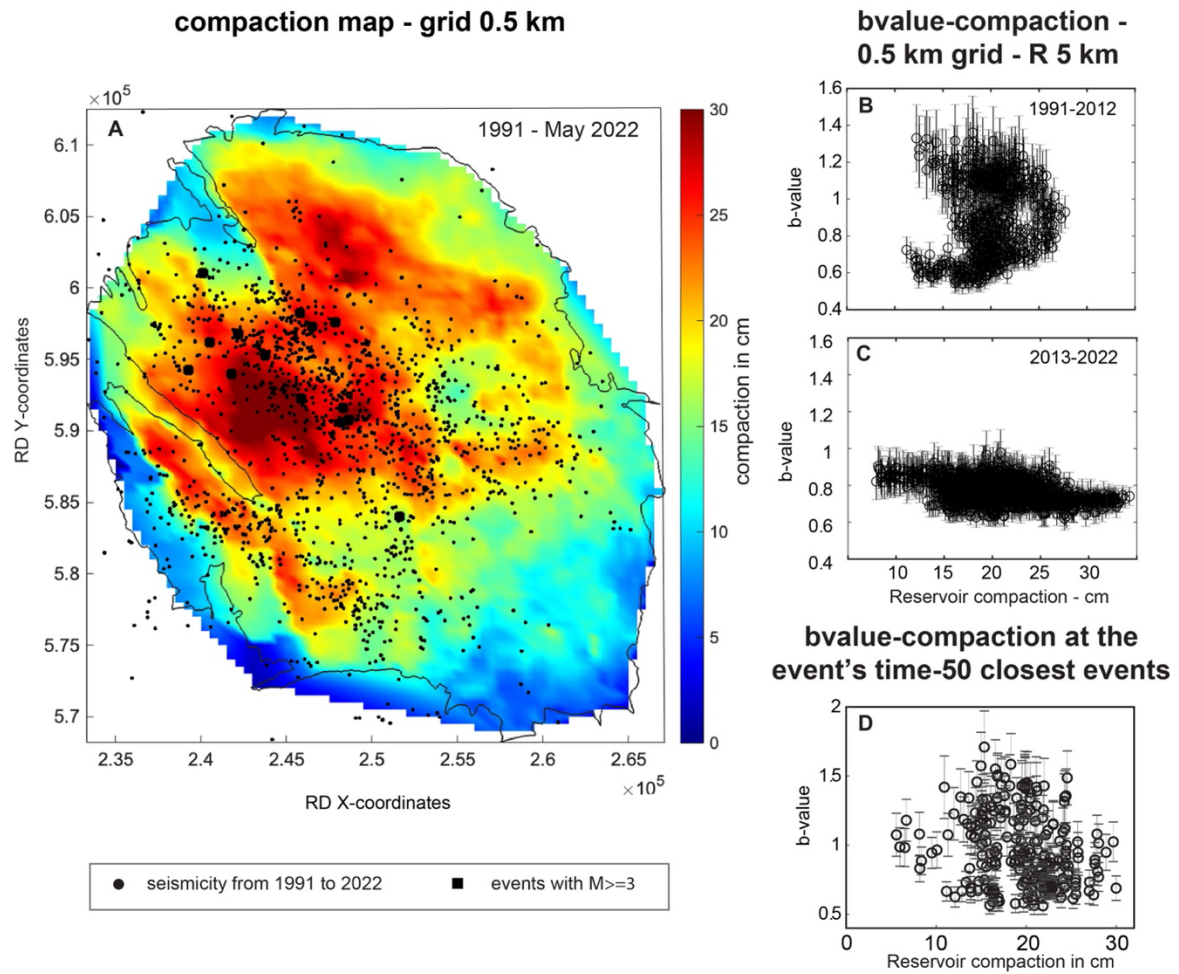
874



875

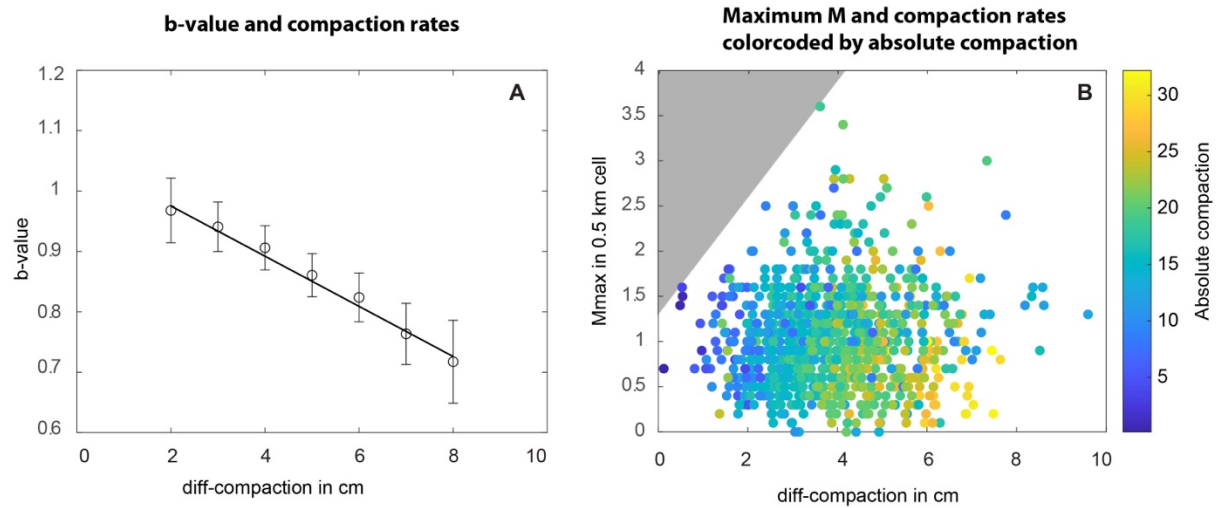
876

877 Figure 8 – **b-value and compaction** - a-c) b-value estimated by AU66 following B2014 on  
 878 subsets of at least 50 events within the range  $\pm 5$  cm of compaction values, for the periods  
 879 1991-2012 (a), 2013-2022 (b) and for the entire period (1991-2022, c). The original  
 880 figure 14 by B2014 is shown as inset in a.  
 881 d-f) comparison between the frequency-magnitude distributions of the minimum and  
 882 maximum b-value for the same periods.



883

884 Figure 9 – **Compaction map and b-value** - a) compaction map: cumulative compaction  
 885 at the year 2022, calibrated on the V6 scenario, operational strategy 2 (OS2; NAM 2021)  
 886 on a grid of 0.5 km with superimposed seismicity from 1991 to May 2022; b-c) b-value  
 887 versus compaction for the same 0.5-km spaced grid for the periods 1991-2012 and 2013-  
 888 2022. Vertical bar: uncertainty by Shi and Bolt (1982); d) b-value calculated for each  
 889 event in the catalog sampling the closest 50 event above  $M_c$  at the origin time versus the  
 890 compaction of the closest grid node. Vertical bar: uncertainty by Shi and Bolt (1982).



891

892 Figure 10 – ***b-value, magnitude, and compaction rates*** - a) Correlation between b-value  
 893 and compaction rates, expressed by the difference in compaction in 10 years before the  
 894 event's origin time. Vertical bar: uncertainty by Shi and Bolt (1982); black solid line:  
 895 linear regression modelling the relationship between b-value and difference in  
 896 compaction ( $b = -0.0424x + 1.067$ ); b) correlation between the maximum magnitude for  
 897 each 0.5 km cell and compaction rates, expressed by the difference in compaction in 10  
 898 years before the event's origin time, color-coded with respect to the absolute compaction.  
 899 Gray area: if production does not result in the exceedance of about 0.35 cm of compaction  
 900 per year, events above M3 do not occur.

901